Distributed Predefined-Time Droop-Free Unified Control Scheme for Parallel Energy Storage Units in All-Electric Aircraft Onboard DC Microgrid

Heyang Yu, Ping Lin, Yuji Zeng, *Graduate Student Member, IEEE*, Qinjin Zhang, *Member, IEEE*, and Yuhu Wu, *Member, IEEE*

***Abstract*—In all-electric aircraft (AEA), onboard dc microgrids with parallel energy storage units (ESUs) often suffer from state-of-charge (SoC) imbalance, inaccurate current distribution, and dc bus voltage instability—threatening system safety and performance. This article proposes a distributed droop-free unified control scheme based on predefined-time (PdT) control theory, addressing these challenges through two main components. First, a distributed PdT consensus observer allows each ESU to locally estimate global average values within user-defined timeframe by exchanging information only with neighboring units. Second, a PdT droop-free unified controller simultaneously achieves precise SoC-based current allocation and stable bus voltage regulation—without relying on droop coefficients or multiple secondary loops. Simulation results under communication delays, controller input noise, and network scalability conditions demonstrate that the proposed method restores bus voltage and synchronizes control variables within a PdT. Compared to enhanced droop-based strategies, it reduces bus voltage fluctuation by up to 80.8%, and significantly improves SoC balancing speed and current distribution accuracy. Hardware-in-the-loop experiments on the Starsim platform validate the method's real-time performance and robustness under load transients and fault conditions. Overall, the proposed scheme offers a scalable, low-complexity solution for reliable coordination control in AEA microgrids with multiple ESUs.**

***Index Terms*—DC microgrid, parallel dc–dc converters, power sharing, state-of-charge (SoC) balancing, voltage regulation.**

I. Introduction

THE transition from mechanically driven to electrically dominated energy systems has accelerated the development of all-electric aircraft (AEA), offering reduced noise, improved efficiency, lower emissions, and enhanced reliability [1], [2]. Prominent projects such as the X57, E-FAN 1.0, and Eviation Alice underscore the growing role of AEA in aviation electrification. In typical AEA architectures, onboard power systems are implemented as dc microgrids powered by sustainable generators (SGs), such as photovoltaic arrays and fuel cells. To ensure reliable power supply, battery energy storage units (ESUs) are deployed for peak shaving and valley filling [3]. Rather than relying on a single high-capacity ESU, employing multiple smaller ESUs in parallel enhances system redundancy, fault tolerance, and design flexibility, while potentially reducing cost [4].

A major challenge in managing parallel ESUs is achieving state-of-charge (SoC)-based current sharing while maintaining stable dc bus voltage. Despite initial SoC alignment, mismatched line impedances and variations in generator output and load demand cause gradual SoC divergence [5]. Without proper SoC thresholds, this imbalance risks overcharge or deep discharge, accelerating degradation and compromising safety. Conversely, rigid thresholds may trigger early ESU disconnection, overloading remaining units and threatening microgrid stability [6]. To address these issues, control strategies—typically categorized as decentralized, centralized, or distributed based on communication requirements—have been extensively studied to enhance current distribution and voltage regulation.

A decentralized approach in [7] utilizes ac small-signal injection to modulate output voltage for power sharing. However, this method is unable to allocate current in accordance with the charge/discharge capacities of individual ESUs, and the injected ac signal adversely affects power quality. To overcome these limitations, the authors in [8] and [9] proposed a droop control scheme wherein the droop coefficient is formulated as a function of the nth power of the SoC, enabling SoC-based power allocation. Despite this improvement, excessive droop coefficients can lead to bus voltage oscillations and compromise system stability. Overall, decentralized strategies rely exclusively on local ESU data. While offering high modularity and system flexibility, the lack of global coordination inherently limits control accuracy and system-level performance.

To incorporate global coordination, [10] proposes a voltage-shifting droop control method, wherein a coupling factor "X" encapsulates aggregated SoC information across ESUs. By

Received 15 April 2025; accepted 22 May 2025. Date of publication 27 May 2025; date of current version 5 August 2025. This work was supported in part by the National Natural Science Foundation of China under Grant 62203085 and in part by the Fundamental Research Funds for the Central Universities under Grant DUT25RC(3)023. Recommended for publication by Associate Editor M. Ferdowsi. *(Corresponding author: Ping Lin.)*

Heyang Yu, Ping Lin, and Yuhu Wu are with the Key Laboratory of Intelligent Control and Optimization for Industrial Equipment of Ministry of Education, and the School of Control Science and Engineering, Dalian University of Technology, Dalian 116024, China (e-mail: heyang.yu@mail.dlut.edu.cn; dmulinping@dlut.edu.cn; wuyuhu@dlut.edu.cn).

Yuji Zeng and Qinjin Zhang are with the College of Marine Engineering, Dalian Maritime University, Dalian 116026, China (e-mail: zengyuji@foxmail.com; zqj20@dlmu.edu.cn).

Color versions of one or more figures in this article are available at https://doi.org/10.1109/TPEL.2025.3573981.

Digital Object Identifier 10.1109/TPEL.2025.3573981

adaptively adjusting "X," the droop characteristics are dynamically modified to facilitate SoC equalization. Similarly, Zhi et al. [11] introduced a virtual dc motor-based control framework that integrates SoC and armature resistance to improve bus voltage regulation and achieve dynamic SoC balancing. While these centralized approaches are relatively straightforward to implement, they suffer from high communication overhead, poor scalability, and vulnerability to single-point failures. Furthermore, neither method accounts for disparities in ESU rated capacities, thereby limiting control accuracy and system reliability.In recent years, distributed droop-based control strategies have attracted considerable attention due to their low communication requirements and inherent robustness against single-point failures. Oliveira et al. [12] proposed a droop adjustment mechanism based on a natural exponential function to promote SoC convergence toward the global average. However, it lacks line impedance compensation and overlooks the heterogeneous rated capacities of ESUs, limiting its power allocation accuracy. To improve current sharing and voltage regulation, Wang et al. [13] introduced proportional–integral (PI) adjustments to the droop coefficients along with secondary controllers, while Hoang and Lee [14] extended this approach for SoC balancing. Similarly, the authors in [15] and [16] developed a multilevel control structure combining adaptive droop tuning with dedicated secondary controllers for line impedance and voltage compensation. Further developments in [17] and [18] employ voltage-shifting strategies to enhance SoC-based current distribution and voltage recovery. Although these methods improve steady-state performance, they generally offer only asymptotic stability, leading to slow dynamic responses under rapid load or generation changes. Moreover, the use of multiple secondary controllers increases system complexity and risks control loop interactions.

To address the aforementioned challenges, Huang et al. [19] integrated bus voltage restoration and line impedance compensation into a simplified control framework. Although this structural refinement reduces the complexity of the control architecture, its dynamic convergence performance remains limited. To improve transient response, Zhang and Hredzak [20] introduced a finite-time (FT) control strategy that accelerates the dynamic behavior of secondary control loops. However, this method relies on precise knowledge of initial system states, which may not be readily obtainable in practical scenarios. To eliminate this dependency, Sahoo et al. [21] proposed a fixed-time (FxT) control strategy that ensures convergence within a predetermined duration, independent of initial conditions. Building on this, Zeng et al. [22] further addressed the limitation of [21] by enabling current allocation based on SoC. Nevertheless, it still falls short of achieving user-defined convergence speeds. Further advancements are presented in [23] and [24], where predefined-time (PdT) control techniques are developed to achieve user-specified convergence times for SoC balancing. Although the methods in [23] and [24] guarantee deterministic convergence speed, they generally suffer from slow SoC balancing and exhibit sensitivity to line impedance mismatches. In addition, their controller design and implementation processes are relatively complex, indicating considerable potential for further improvement.

It is well recognized that most existing methods adopt droop-based control strategies that leverage virtual impedance for current distribution and voltage regulation. However, these approaches inherently suffer from a fundamental tradeoff: low virtual impedance compromises current sharing accuracy, while high virtual impedance induces considerable bus voltage deviations, thereby jeopardizing system stability and operational safety. To address this issue, a limited number of distributed droop-free control strategies have been proposed. For example, Moayedi et al. [25] presented a droop-free power allocation approach that eliminates the dependence on virtual impedance, and its robustness against line impedance mismatches is further enhanced in [26]. Despite these advancements, the authors in [25] and [26] lacked the capability for SoC-based current allocation and exhibit limited convergence speed. These limitations highlight the need for more advanced control methods capable of achieving both PdT dynamic response and accurate SoC-based power distribution.

The above-mentioned methods are summarized and compared in Table I. While prior studies have contributed significantly to SoC-based current distribution and voltage regulation in parallel ESUs, several key challenges remain unresolved as follows:

1) How to resolve the inherent tradeoff between current sharing and voltage restoration in conventional droop-based control strategies?
2) How to integrate multiple control objectives—namely, SoC balancing, current sharing, and voltage recovery—into a unified control framework with a simplified structure?
3) How to improve the dynamic performance of the control system while reducing the complexity of parameter tuning and achieving fast SoC equalization?

Motivated by the above-mentioned observations, this article focuses on the coordinated control of multiple parallel ESUs in dc microgrids onboard AEA, and proposes a distributed PdT droop-free unified control scheme. The main contributions are summarized as follows:

1) A novel droop-free control strategy is proposed to eliminate reliance on virtual droop resistances. Unlike conventional droop-based methods that tradeoff current sharing accuracy for bus voltage stability, the proposed approach ensures precise current distribution while substantially suppressing bus voltage fluctuations, thereby enhancing system reliability under dynamic conditions.
2) Compared to conventional droop-based and existing droop-free strategies, the proposed unified framework simultaneously achieves SoC balancing, current sharing, and bus voltage regulation without relying on multiple secondary controllers. This integration simplifies the control structure, enhances scalability, and mitigates instability risks arising from interactions among layered control loops in large-scale ESU systems.
3) Built upon PdT control theory, the proposed scheme integrates a distributed PdT consensus observer with a PdT-based unified controller. This design enables each ESU to locally estimate averages through neighbor-to-neighbor communication and achieve reference tracking within a

TABLE I
COMPARISON OF EXISTING COORDINATED CONTROL METHODS FOR MULTIPLE PARALLEL ESUS

Method	Communication reliance	Whether droop-free	SoC balance capability	SoC balancing speed	Controllers settling time	Number of outer controllers	Voltage recovery	Scalability test	Sensitivity to line impedance mismatch
[7]	No	✘	✘	None	Infinite	1	✘	✘	Low
[8]	No	✘	✓	Slow	Infinite	1	✘	✘	High
[9]	No	✘	✓	Slow	Infinite	1	✘	✘	High
[10]	High	✘	✓	Slow	Infinite	1	✘	✘	High
[11]	High	✘	✓	Slow	Infinite	1	✘	✘	High
[12]	Low	✘	✓	Slow	Infinite	2	✘	✘	High
[13]	Low	✘	✘	None	Infinite	3	✓	✘	Low
[14]	Low	✘	✓	Slow	Infinite	3	✓	✘	Low
[15]	Low	✘	✓	Fast	Infinite	3	✓	✘	Low
[16]	Low	✘	✓	Slow	Infinite	3	✓	✘	Low
[17]	Low	✘	✓	Slow	Infinite	2	✓	✓	Low
[18]	Low	✘	✓	Slow	Infinite	2	✓	✘	Low
[19]	Low	✘	✓	Fast	Infinite	2	✓	✘	Low
[20]	Low	✘	✓	Slow	Finite	1	✓	✘	Low
[21]	Low	✘	✘	None	Fixed	3	✓	✘	Low
[22]	Low	✘	✓	Fast	Fixed	1	✓	✓	Low
[23]	Low	✘	✓	Slow	Pre-defined	1	✘	✘	High
[24]	Low	✘	✓	Slow	Pre-defined	2	✓	✘	High
[25]	Low	✓	✘	None	Infinite	1	✘	✘	High
[26]	Low	✓	✘	None	Infinite	1	✓	✘	Low
Proposed	Low	✓	✓	Fast	Pre-defined	1	✓	✓	Low

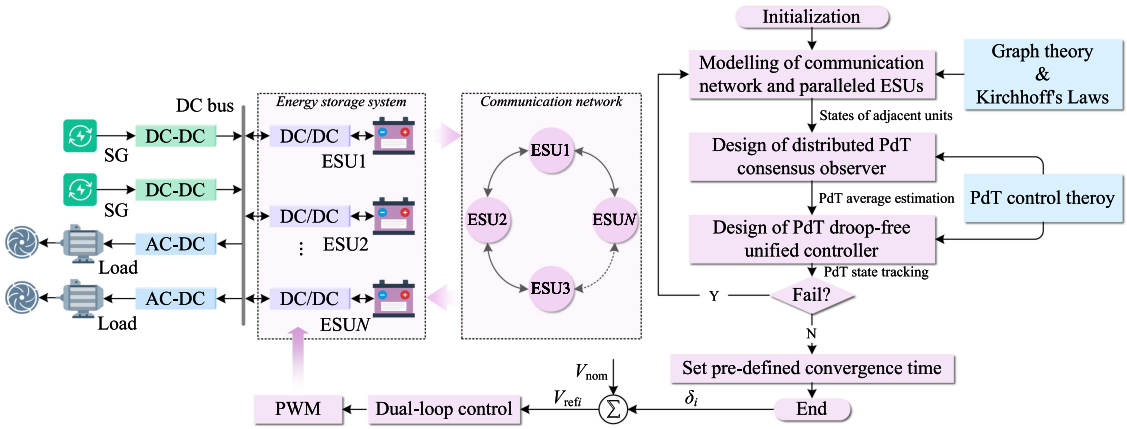

Fig. 1. Preview of the methodology and design process of the proposed distributed droop-free unified control strategy for parallel ESUs in AEA onboard DC microgrid.

user-defined time, while simplifying parameter tuning and implementation. By embedding SoC and current information into redesigned virtual variables, the scheme accelerates SoC equalization and maintains robustness against line impedance mismatches.

The rest of this article is organized as follows. Section II introduces the overall methodology, the AEA onboard dc microgrid, and the PdT control theory. Section III details the design and analysis of the proposed distributed PdT droop-free unified control scheme. Section IV evaluates the scheme's effectiveness and robustness through simulation studies and performance comparisons with existing methods. Section V presents experimental validation. Finally, Section VI concludes this article.

II. SYSTEM DESCRIPTION AND PRELIMINARIES

A. AEA DC Microgrid Structure and Overall Methodology

The proposed scheme is designed for multiple ESUs in the AEA onboard dc microgrid. As illustrated in Fig. 1, each ESU is interfaced with the dc bus through a dc/dc converter, serving as an auxiliary power source. These units store surplus energy generated by the SGs and provide supplementary power as required, thereby ensuring stable system operation.

Fig. 1 also depicts the overall flow diagram of the proposed control method for the ith ESU. During the theoretical design phase, the equivalent circuit of multiple parallel ESUs is first modeled using Kirchhoff's laws, while the distributed communication network is described using graph theory. Based on PdT control theory, a distributed PdT-based observer is developed to enable each ESU to estimate the average of relevant variables within the communication network through local computation and neighbor communication. Meanwhile, a PdT droop-free unified controller is designed to generate the reference input for the dual-loop control of the dc/dc converter, effectively addressing challenges, such as SoC imbalance, inaccurate current distribution, and bus voltage deviations. Notably, once the control scheme is designed, users only need to specify a predefined convergence time and tune the dual-loop control parameters, eliminating the need for further adjustments.

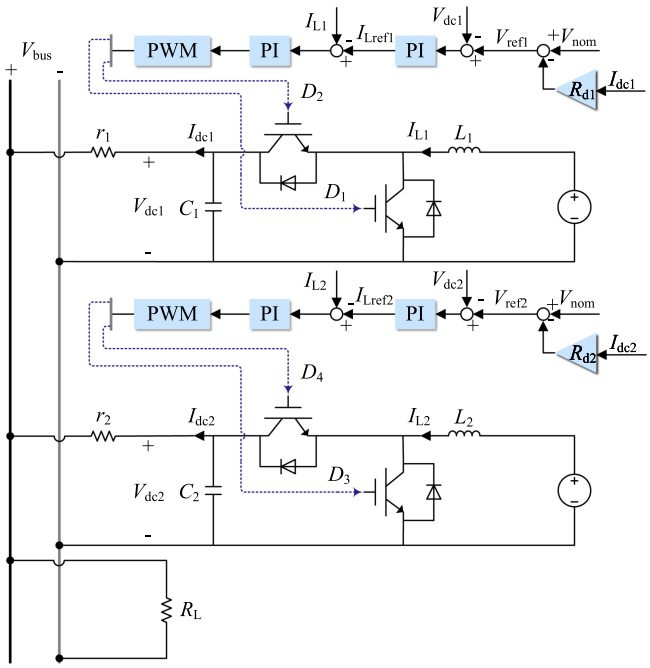

Fig. 2. Simplified model of two ESUs operating in droop control mode connected in parallel.

B. Limitations of Droop-Based Methods for Paralleled ESUs

Droop control is a widely adopted method for current distribution among parallel ESUs. Consider the case where two ESUs with droop control are connected in parallel. The equivalent circuit is shown in Fig. 2.

The output voltage of ESUs are assumed to rapidly track the reference output voltage, attributed to the rapid response characteristics of the voltage and current dual closed-loop control [27]

$$V_{\mathrm{dc}i} = V_{\mathrm{ref}i} \tag{1}$$

where $V_{\mathrm{ref}i}$ is the reference output voltage, $V_{\mathrm{dc}i}$ is the output voltage of ESU. By applying Kirchhoff's voltage law [28], there is

$$V_{\mathrm{bus}} = V_{\mathrm{dc}i} - I_{\mathrm{dc}i} r_i \tag{2}$$

where $I_{\mathrm{dc}i}$, V_{bus}, and r_i represent output current of ESU, bus voltage, and line resistance, respectively.

Under droop control, the reference output voltage of each ESU is given by

$$V_{\mathrm{ref}i} = V_{\mathrm{nom}} - I_{\mathrm{dc}i} R_{\mathrm{d}i} \tag{3}$$

where $R_{\mathrm{d}i}$ is droop coefficient. Simultaneously, defining the capacity-weighted current

$$I_{\mathrm{b}i} \triangleq \frac{I_{\mathrm{dc}i}}{C_{\mathrm{b}i}} \tag{4}$$

where $C_{\mathrm{b}i}$ is rated capacity.

The SoC of a battery can be estimated using the Coulomb counting method

$$\dot{S}_i = -\mu I_{\mathrm{b}i}, S_i(0) = S_{i\_0} \tag{5}$$

where S_i, S_{i_0}, and μ, are instantaneous SoC, initial SoC, and voltage gain of ESU converter.

Combining (1) to (5), the ratio of SoC changing rates of between two ESUs can be obtained as follows:

$$\frac{\dot{S}_1}{\dot{S}_2} = \frac{(R_{\mathrm{d}2} + r_2) C_{\mathrm{b}2}}{(R_{\mathrm{d}1} + r_1) C_{\mathrm{b}1}}. \tag{6}$$

Remark 1: Equation (6) indicates that conventional droop control fails to maintain dynamic SoC balance when line impedances and rated capacities are mismatched. To address this limitation, existing methods integrate SoC information into the droop control framework, improving SoC balance among parallel ESUs. However, these approaches rely on additional secondary controllers to mitigate line impedance mismatch effects on current sharing and to compensate for dc bus voltage deviations caused by droop coefficients and line impedance. The inclusion of secondary controllers increases system complexity, potentially leading to control instability and scalability issues in multi-ESU configurations, which can compromise the stable operation of AEA onboard dc microgrids. Therefore, a simplified yet robust control strategy that ensures dynamic SoC balance, proportional load current sharing, and stable dc bus voltage regulation remains a critical challenge in advancing AEA onboard dc microgrid technology.

C. Communication Network Based on Graph Theory

As discussed earlier, centralized control schemes impose substantial communication overhead and face scalability challenges as the system size increases. To enhance control performance while minimizing communication demands, a distributed communication network is essential.

In practical applications, the communication network of AEA DC microgrids typically employs the CAN bus protocol to facilitate efficient data exchange. To better describe the constructed sparse communication network, this section applies graph theory, modeling each ESU as an agent within a sparse ring topology, denoted as $\boldsymbol{\mathcal{G}} = \{\boldsymbol{\mathcal{V}}, \boldsymbol{\mathcal{E}}, \boldsymbol{\mathcal{A}}\}$. Agents execute local computations, exchange information with adjacent nodes, and collaborate to achieve consistent control objectives [29]. Within the graph $\boldsymbol{\mathcal{G}}$, the following properties and lemmas hold.

- The node set $\boldsymbol{\mathcal{V}} = \{\mathrm{ESU}1, \mathrm{ESU}2, \ldots, \mathrm{ESU}N\}$ where ESUi is the ith node and $i \in \boldsymbol{\mathcal{I}} = \{1, 2, \ldots, N\}$, the edge set $\boldsymbol{\mathcal{E}} \subseteq \boldsymbol{\mathcal{V}} \times \boldsymbol{\mathcal{V}}$ indicates that if ESUi and ESU$j (j \in \boldsymbol{\mathcal{I}})$ can exchange information, there is an edge between them, denoted by $\mathcal{E}_{ij} = (\mathrm{ESU}i, \mathrm{ESU}j) \in \boldsymbol{\mathcal{E}}$. If $\boldsymbol{\mathcal{G}}$ is weighted, the set of neighbors of ESUi is represented by $\boldsymbol{\mathcal{N}}_i = \{j | (\mathrm{ESU}i, \mathrm{ESU}j) \in \boldsymbol{\mathcal{E}}\}$.
- The related adjacency matrix $\boldsymbol{\mathcal{A}} \in \mathbb{R}^{N \times N}$ is composed of communication weights a_{ij}. $a_{ij} = 1$ if the agent j can transmit information to agent i, otherwise $a_{ij} = 0$. Meanwhile, the degree matrix is described as $\boldsymbol{\mathcal{D}} = \mathrm{diag}\{d_i\} \in \mathbb{R}^{N \times N}$, $d_i = \sum_{j \in \boldsymbol{\mathcal{N}}_i} a_{ij}$, and the Laplacian matrix is constructed as $\boldsymbol{\mathcal{L}}(\boldsymbol{\mathcal{A}}) = \boldsymbol{\mathcal{D}} - \boldsymbol{\mathcal{A}} \in \mathbb{R}^{N \times N}$.

Lemma 1 [30]: For an undirected connected graph $\boldsymbol{\mathcal{G}}$, the Laplacian matrix $\boldsymbol{\mathcal{L}}(\boldsymbol{\mathcal{A}})$ has the following properties.

1) $\mathcal{L}(\mathcal{A})$ is a semipositive-definite matrix, and all eigenvalues of $\mathcal{L}(\mathcal{A})$ are real and nonnegative.
2) If $\mathcal{G}$ is connected, the second smallest eigenvalue of $\mathcal{L}(\mathcal{A})$, denoted by λ, is larger than 0. Furthermore, the following holds:

$$\boldsymbol{x}^T \mathcal{L}(\mathcal{A})\boldsymbol{x} = \frac{1}{2}\sum_{i,j=1}^{N} a_{ij}(x_i - x_j)^2$$

$$\boldsymbol{x}^T \mathcal{L}(\mathcal{A})\,\boldsymbol{x} \geq \lambda \boldsymbol{x}^T \boldsymbol{x}.$$

Lemma 2 [31]: For a weighted undirected graph, if $F(x_i, x_j) : \mathbb{R}^2 \to \mathbb{R}$ is an odd function, the following relationship is established:

$$\sum_{i,j=1}^{N} a_{ij} x_i F(x_i, x_j) = \frac{1}{2}\sum_{i,j=1}^{N} a_{ij}(x_i - x_j) F(x_i, x_j).$$

D. Preliminaries of PdT Control Theory

Consider the following system:

$$\dot{\boldsymbol{x}} = f(\boldsymbol{x}, t), \boldsymbol{x}(0) = \boldsymbol{x}_0 \tag{7}$$

where $\boldsymbol{x} \in \mathbb{R}^N$ denotes the system's state variable vector, $\boldsymbol{x}_0 \in \mathbb{R}^N$ denotes the initial state variable vector, and $f(\boldsymbol{x}, t) \in \mathbb{R}^N \times \mathbb{R}^+ \to \mathbb{R}^N$ is nonlinear. For a general nonlinear system (7), the following definitions hold.

Definition 1: If the origin of (7) is Lyapunov stable and every solution $\boldsymbol{x}(t, \boldsymbol{x}_0)$ reaches equilibrium within a finite settling time $T(\boldsymbol{x}_0) \in \mathbb{R}^N \to \mathbb{R}$, then the origin is globally FT stable.

Definition 2: If the origin is globally FT stable with a bounded settling time $T(\boldsymbol{x}_0)$, then it is FxT stable, ensuring there is a maximum time $T_{\max}$ such that $T(\boldsymbol{x}_0) \leq T_{\max}$ for any initial state.

Definition 3: If the origin is FxT stable, with the settling time is bounded by $T(\boldsymbol{x}_0) \leq T_c$, where T_c denotes the user-defined convergence time upper bound, then it is PdT stable.

Lemma 3 [32]: If a continuous, positive definite, radially unbounded function $V(\boldsymbol{x})$ exists for (7) and it satisfies

$$\dot{V} \leq -\frac{2}{\sigma T_c}\left(2V + V^{\frac{2-\sigma}{2}} + V^{\frac{2+\sigma}{2}}\right)$$

where $\sigma \in (0, 1)$ is a real constant. Then, the origin of system (7) is globally PdT stable, and the settling time function $T(\boldsymbol{x}_0)$ complies to

$$T(\boldsymbol{x}_0) \leq T_c\left(1 - \frac{1}{1 + V(\boldsymbol{x}_0)^{\frac{\sigma}{2}}}\right) \leq T_c.$$

Lemma 4 [33]: Let $\chi_1, \chi_2, \ldots, \chi_N \geq 0$, $p \in (0, 1]$ and $q \in [1, \infty)$, then

$$\sum_{i=1}^{N} \chi_i^p \geq \left(\sum_{i=1}^{N} \chi_i\right)^p$$

$$\sum_{i=1}^{\mathcal{N}} \chi_i^q \geq N^{1-q}\left(\sum_{i=1}^{N} \chi_i\right)^q.$$

III. Design of Distributed PdT Droop-Free Unified Control Scheme

This section begins by presenting the control objectives and the overall structure of the proposed strategy. Subsequently, a distributed PdT consensus observer and a PdT-based droop-free unified controller are developed and rigorously analyzed. These components are designed to integrate proportional current distribution, dynamic SoC balancing, and bus voltage restoration within a unified framework. Finally, a detailed description of the implementation procedure for the proposed control scheme is provided.

A. Control Objectives and Structure

Improved droop-based strategies often increase complexity and communication demands, and lead to ESU instability due to multiloop coupling and bus voltage fluctuations. A simplified and reliable control scheme is crucial to effectively address SoC imbalance, current inaccuracies, and voltage deviations. In response to these challenges, the reference voltage for ESUi is introduced

$$V_{\text{ref}i} = V_{\text{nom}} + \delta_i \tag{8}$$

where V_{nom} and δ_i are rated dc bus voltage and the droop-free unified controller to be designed, respectively.

From (1), (2), and (8), the following droop-free control paradigms for each ESU can be constructed:

$$\dot{V}_{\text{bus}} = u_i^{\text{V}} \tag{9}$$

$$\dot{I}_{\text{dc}i} = G_i u_i^{\text{I}} \tag{10}$$

where u_i^{V} and u_i^{I} are the control laws responsible for voltage restoration and current distribution, respectively. $G_i = 1/r_i$ is the line conductance of ith ESU.

In light of (5), (10) can be reformulated as follows:

$$\dot{\vartheta}_i = G_i u_i^{\vartheta} \tag{11}$$

where ϑ_i represents a virtual variable that is associated with both SoC balancing and current distribution, which needs to be designed. Its derivative satisfy

$$\dot{\vartheta}_i = \dot{I}_{\text{dc}i} = -\frac{C_{\text{b}i}\ddot{S}_i}{\mu}.$$

Referring to (9) and (11), the droop-free unified controller can be formulated

$$\dot{\delta}_i = u_i^{\vartheta} + u_i^{\text{V}}. \tag{12}$$

Remark 2: It can be observed that the design of the control law u_i^{ϑ} is closely related to the line conductance G_i, which is typically assumed to be precisely known during control law design, as noted in [34] and [35]. However, in practical scenarios, accurately determining G_i is challenging due to limitations in measurement techniques, as well as constraints related to the precision and cost of sensing equipment. To better reflect real-world conditions, this article assumes that the exact value of G_i in the AEA dc microgrid is unavailable when designing

u_i^{ϑ}. Instead, only an approximate limits $[G_{\min}, G_{\max}]$ is assumed to be known, where $G_{\min}$ and $G_{\max}$ denote the known lower and upper limits, respectively. This assumption aligns with practical constraints while ensuring the stability of the controller in subsequent designs. To further account for extreme conditions in which even $G_{\min}$ is unknown and enhance the practical applicability of the proposed control scheme, a conservative value of $G_{\min}$ is assigned as $G_{\min} = I_{\max}/(0.05V_{\text{nom}})$ under such conditions, where $I_{\max}$ is the maximum rated current of all parallel-connected converters.

Now it is ready to present the control objectives as follows.

1) The global averages of virtual variables and SoCs can be observed within the predefined settling time

$$\lim_{t\to T_c} |S_{ai}(t) - S_{aj}(t)| \to 0$$
$$\lim_{t\to T_c} |\vartheta_{ai}(t) - \vartheta_{aj}(t)| \to 0 \tag{13}$$

where S_{ai}, ϑ_{ai}, S_{aj}, and ϑ_{aj} are the average SoC and virtual variable observed locally in ESUi and ESUj, respectively.

2) The virtual variables must approach the global average within the predefined settling time to facilitate dynamic SoC balancing and proportional current distribution

$$\lim_{t\to T_c} |\vartheta_i(t) - \vartheta_{ai}(t)| \to 0. \tag{14}$$

3) The bus voltage must be restored to its nominal value within a predefined settling time

$$\lim_{t\to T_c} |V_{\text{bus}}(t) - V_{\text{nom}}| \to 0. \tag{15}$$

To achieve the aforementioned control objectives, a more concise droop-free unified control architecture based on PdT control theory is proposed. Fig. 3 compares the proposed architecture with a droop-based improved scheme. The latter employs independent PI controllers for each control objective, leading to potential control loop interactions. In contrast, the proposed unified control architecture eliminates the destabilizing effects of traditional droop control on bus voltage stability [16]. By integrating all control objectives into a single controller, it mitigates the coupling effects associated with multiple control loops, simplifies parameter tuning, and enhances overall system stability.

B. Distributed PdT Consensus Observer

As observed in Fig. 3, the fast and precise estimation of the S_{ai} and ϑ_{ai} plays a crucial role in the proportional current distribution, dynamic SoC balancing, and bus voltage restoration for each ESU. Without loss of generality, let y_i and y_j denote the state variables to be observed in ESUi and ESUj, a distributed PdT consensus observer is proposed as follows:

$$\dot{y}_i(t) = -\kappa_1 \sum_{j\in\mathcal{N}_i} a_{ij}\left(y_i(t) - y_j(t)\right) - \kappa_2 \sum_{j\in\mathcal{N}_i} a_{ij}\left(y_i(t) - y_j(t)\right)^{\lceil 1-\sigma\rfloor}$$

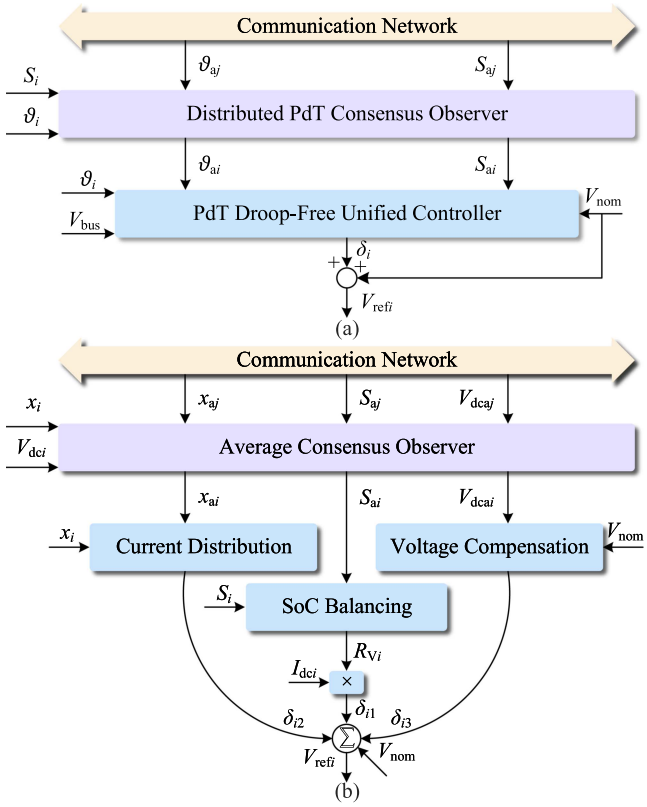

Fig. 3. Comparison of the control architectures between the proposed method and the improved strategies based on traditional droop control.

$$- \kappa_3 \sum_{j\in\mathcal{N}_i} a_{ij}\left(y_i(t) - y_j(t)\right)^{\lceil 1+\sigma\rfloor} \tag{16}$$

where $(\cdot)^{\lceil\varpi\rfloor} \triangleq \text{sgn}(\cdot)|\cdot|^{\varpi}$, and

$$\kappa_1 = \frac{2}{\sigma T_c}\lambda^{-1}$$
$$\kappa_2 = \frac{1}{\sigma T_c} 4^{\frac{\sigma}{2}} \lambda^{\frac{-2+\sigma}{2}}$$
$$\kappa_3 = \frac{1}{\sigma T_c} 4^{\frac{-\sigma}{2}} N^{\frac{\sigma}{2}} \lambda^{\frac{-2-\sigma}{2}}. \tag{17}$$

Theorem 1: If the control law of the consensus observer is designed in accordance with (16), it will be PdT stable.

Proof: Let the average value of the ith agent be $y^* = \frac{1}{N}\sum_{i=1}^{N} y_i$ and denote the state variable mismatch of the ith agent as $\varepsilon_i = y_i - y^*$. The Lyapunov candidate function is given by

$$V_{\Xi} = \frac{1}{2}\boldsymbol{\varepsilon}^T\boldsymbol{\varepsilon}$$

where $\boldsymbol{\varepsilon} = [\varepsilon_1, \varepsilon_2, \ldots, \varepsilon_N]^T \in \mathbb{R}^N$ represents the vector of state variable mismatch.

For a weighted undirected graph, it holds that $\sum_{i=1}^{N} \dot{y}_i = 0$. Consequently, the time derivative of the state variable mismatch for the ith agent is $\dot{\varepsilon}_i = \dot{y}_i$. Differentiating V_{ε} with respect to

time yields

$$\begin{aligned}\dot{V}_{\Xi} &= \sum_{i=1}^{N} \varepsilon_i \dot{\varepsilon}_i \\ &= \mathscr{V}_{\Xi 1} + \mathscr{V}_{\Xi 2} + \mathscr{V}_{\Xi 3}\end{aligned}$$

where

$$\begin{aligned}\mathscr{V}_{\Xi 1} &= -\kappa_1 \sum_{i=1}^{N} \varepsilon_i \left(\sum_{j \in \boldsymbol{\mathcal{N}}_i} a_{ij} \left(\varepsilon_i - \varepsilon_j \right) \right) \\ \mathscr{V}_{\Xi 2} &= -\kappa_2 \sum_{i=1}^{N} \varepsilon_i \left(\sum_{j \in \boldsymbol{\mathcal{N}}_i} a_{ij} \left(\varepsilon_i - \varepsilon_j \right)^{\lceil 1-\sigma \rfloor} \right) \\ \mathscr{V}_{\Xi 3} &= -\kappa_3 \sum_{i=1}^{N} \varepsilon_i \left(\sum_{j \in \boldsymbol{\mathcal{N}}_i} a_{ij} \left(\varepsilon_i - \varepsilon_j \right)^{\lceil 1+\sigma \rfloor} \right). \end{aligned} \tag{18}$$

Applying Lemma 2 and Lemma 4, (18) can be derived as follows:

$$\begin{aligned}\mathscr{V}_{\Xi 1} &= -\frac{1}{2}\kappa_1 \sum_{i,j=1}^{N} a_{ij} \left| \varepsilon_i - \varepsilon_j \right|^2 \\ \mathscr{V}_{\Xi 2} &= -\frac{1}{2}\kappa_2 \sum_{i,j=1}^{N} \left(a_{ij}{}^{\frac{2}{2-\sigma}} \left| \varepsilon_i - \varepsilon_j \right|^2 \right)^{\frac{2-\sigma}{2}} \\ &\leq -\frac{1}{2}\kappa_2 \left(\sum_{i,j=1}^{N} a_{ij}{}^{\frac{2}{2-\sigma}} \left| \varepsilon_i - \varepsilon_j \right|^2 \right)^{\frac{2-\sigma}{2}} \\ \mathscr{V}_{\Xi 3} &= -\frac{1}{2}\kappa_3 \sum_{i,j=1}^{N} \left(a_{ij}{}^{\frac{2}{2+\sigma}} \left| \varepsilon_i - \varepsilon_j \right|^2 \right)^{\frac{2+\sigma}{2}} \\ &\leq -\frac{1}{2}\kappa_3 N^{-\frac{\sigma}{2}} \left(\sum_{i,j=1}^{N} a_{ij}{}^{\frac{2}{2+\sigma}} \left| \varepsilon_i - \varepsilon_j \right|^2 \right)^{\frac{2+\sigma}{2}}. \end{aligned}$$

Given the properties of graph $\boldsymbol{\mathcal{G}}$, where a_{ij} is either 1 or 0, it follows that $a_{ij} = a_{ij}{}^{\frac{2}{2-\sigma}} = a_{ij}{}^{\frac{2}{2+\sigma}}$. Therefore, $\boldsymbol{\mathcal{L}}(\boldsymbol{\mathcal{A}}) = \boldsymbol{\mathcal{L}}(\boldsymbol{\mathcal{A}}_1) = \boldsymbol{\mathcal{L}}(\boldsymbol{\mathcal{A}}_2)$. Subsequently, using Lemma 1

$$\begin{aligned}\mathscr{V}_{\Xi 1} &\leq -\frac{1}{2}\kappa_1 \left(2\boldsymbol{\varepsilon}^T \boldsymbol{\mathcal{L}}\left(\boldsymbol{\mathcal{A}}\right) \boldsymbol{\varepsilon} \right) \\ &\leq -\frac{1}{2}\kappa_1 \left(2\lambda \boldsymbol{\varepsilon}^T \boldsymbol{\varepsilon} \right) \\ \mathscr{V}_{\Xi 2} &\leq -\frac{1}{2}\kappa_2 \left(2\boldsymbol{\varepsilon}^T \boldsymbol{\mathcal{L}}\left(\boldsymbol{\mathcal{A}}_1\right) \boldsymbol{\varepsilon} \right)^{\frac{2-\sigma}{2}} \\ &\leq -\frac{1}{2}\kappa_2 \left(2\lambda \boldsymbol{\varepsilon}^T \boldsymbol{\varepsilon} \right)^{\frac{2-\sigma}{2}} \\ \mathscr{V}_{\Xi 3} &\leq -\frac{1}{2}\kappa_3 N^{-\frac{\sigma}{2}} \left(2\boldsymbol{\varepsilon}^T \boldsymbol{\mathcal{L}}\left(\boldsymbol{\mathcal{A}}_2\right) \boldsymbol{\varepsilon} \right)^{\frac{2+\sigma}{2}} \\ &\leq -\frac{1}{2}\kappa_3 N^{-\frac{\sigma}{2}} \left(2\lambda \boldsymbol{\varepsilon}^T \boldsymbol{\varepsilon} \right)^{\frac{2+\sigma}{2}}. \end{aligned}$$

From (17), $\dot{V}_{\Xi}$ results in

$$\dot{V}_{\Xi} \leq -\frac{2}{\sigma T_{\mathrm{c}}} \left(2V_{\Xi} + V_{\Xi}^{\frac{2-\sigma}{2}} + V_{\Xi}^{\frac{2+\sigma}{2}} \right).$$

Based on Lemma 3, the designed distributed consensus observer is said to be PdT stable. ■

Remark 3: The PdT stability of the consensus observer reveals that final agreement of the states will satisfy

$$\begin{aligned}\lim_{t \to T_{\mathrm{c}}} \left| y_i(t) - y_j(t) \right| &\to 0 \\ \lim_{t \to T_{\mathrm{c}}} y_i(t) &\to \frac{1}{N} \sum_{i=1}^{N} y_i(0)\end{aligned}$$

which means the average-consensus problem is solved within a PdT.

C. PdT Droop-Free Unified Controller

To achieve rapid SoC-based current distribution, the reconfiguration process of ϑ_i is described as follows:

$$\begin{aligned}\vartheta_i &= \frac{I_{\mathrm{b}i}}{\tanh\left(\gamma_i \Delta S_i\right) + 1} \\ \gamma_i &= \frac{1}{\left|\Delta S_i\right| + \nu}\end{aligned}$$

where $\Delta S_i = S_i - S_{\mathrm{a}i}$, γ_i represents the acceleration factor. When the deviation of S_i from the average is significant, γ_i offers a lower gain to prevent an excessive response during the initial stage of SoC balancing. As S_i approaches the average, γ_i progressively increases the gain, which accelerates SoC balancing in the subsequent stages. The gain range provided by γ_i can be qualitatively adjusted via the parameter ν.

Building upon this, to achieve (14), the related control law u_i^{ϑ} is proposed

$$u_i^{\vartheta} = -\frac{K_1}{G_{\min}} E_{\vartheta i} - \frac{K_2}{G_{\min}} E_{\vartheta i}^{\lceil 1-\sigma \rfloor} - \frac{K_3}{G_{\min}} E_{\vartheta i}^{\lceil 1+\sigma \rfloor} \tag{19}$$

where $E_{\vartheta i} = \vartheta_i - \vartheta_{\mathrm{a}i}$, and

$$\begin{aligned}K_1 &= \frac{2}{\sigma T_{\mathrm{c}}} \\ K_2 &= \frac{1}{\sigma T_{\mathrm{c}}} 2^{\frac{\sigma}{2}} \\ K_3 &= \frac{1}{\sigma T_{\mathrm{c}}}.\end{aligned} \tag{20}$$

Similarly, the control law u_i^{V} correlated with control objective (15) is also proposed as follows:

$$u_i^{\mathrm{V}} = -K_1 E_{\mathrm{V}i} - K_2 E_{\mathrm{V}i}^{\lceil 1-\sigma \rfloor} - K_3 E_{\mathrm{V}i}^{\lceil 1+\sigma \rfloor} \tag{21}$$

where $E_{\mathrm{V}i} = V_{\mathrm{bus}} - V_{\mathrm{nom}}$. It is clear that (12) can be obtained with reference to (19) and (21).

Theorem 2: If the droop-free unified controller is designed according to control laws (19) and (21), it will be PdT stable.

Proof: Select the following Lyapunov candidate:

$$V_{\Delta i} = V_{\vartheta} + V_{\mathrm{V}}$$

where

$$V_\vartheta = \frac{1}{2}E_{\vartheta i}^2$$

$$V_{\mathrm{V}} = \frac{1}{2}E_{\mathrm{V}i}^2.$$

With reference to (9) and (11), the differentiation of $V_{\Delta i}$ is performed as follows:

$$\begin{aligned}\dot{V}_{\Delta i} &= E_{\vartheta i}\dot{E}_{\vartheta i} + E_{\mathrm{V}i}\dot{E}_{\mathrm{V}i} \\ &= -\frac{G_i K_1}{G_{\min}}|E_{\vartheta i}|^2 - \frac{G_i K_2}{G_{\min}}|E_{\vartheta i}|^{2-\sigma} - \frac{G_i K_3}{G_{\min}}|E_{\vartheta i}|^{2+\sigma} \\ &\quad - K_1|E_{\mathrm{V}i}|^2 - K_2|E_{\mathrm{V}i}|^{2-\sigma} - K_3|E_{\mathrm{V}i}|^{2+\sigma} \\ &= -K_1\left(\frac{G_i}{G_{\min}}|E_{\vartheta i}|^2 + |E_{\mathrm{V}i}|^2\right) \\ &\quad - K_2\left(\frac{G_i}{G_{\min}}|E_{\vartheta i}|^2 + |E_{\mathrm{V}i}|^2\right)^{2-\sigma} \\ &\quad - K_3\left(\frac{G_i}{G_{\min}}|E_{\vartheta i}|^2 + |E_{\mathrm{V}i}|^2\right)^{2+\sigma}.\end{aligned}$$

Due to $G_{\min} \le G_i$, there is

$$\begin{aligned}\dot{V}_{\Delta i} &\le -K_1\left(|E_{\vartheta i}|^2 + |E_{\mathrm{V}i}|^2\right) - K_2\left(|E_{\vartheta i}|^{2-\sigma} + |E_{\mathrm{V}i}|^{2-\sigma}\right) \\ &\quad - K_3\left(|E_{\vartheta i}|^{2+\sigma} + |E_{\mathrm{V}i}|^{2+\sigma}\right) \\ &= -2K_1(V_\vartheta + V_{\mathrm{V}}) - 2^{\frac{2-\sigma}{2}}K_2\left(V_\vartheta^{\frac{2-\sigma}{2}} + V_{\mathrm{V}}^{\frac{2-\sigma}{2}}\right) \\ &\quad - 2^{\frac{2+\sigma}{2}}K_3\left(V_\vartheta^{\frac{2+\sigma}{2}} + V_{\mathrm{V}}^{\frac{2+\sigma}{2}}\right).\end{aligned}$$

Applying Lemma 4, it can be obtained that

$$\begin{aligned}\dot{V}_{\Delta i} &\le -2K_1(V_\vartheta + V_{\mathrm{V}}) - 2^{\frac{2-\sigma}{2}}K_2(V_\vartheta + V_{\mathrm{V}})^{\frac{2-\sigma}{2}} \\ &\quad - 2K_3(V_\vartheta + V_{\mathrm{V}})^{\frac{2+\sigma}{2}} \\ &= -2K_1V_{\Delta i} - 2^{\frac{2-\sigma}{2}}K_2V_{\Delta i}^{\frac{2-\sigma}{2}} - 2K_3V_{\Delta i}^{\frac{2+\sigma}{2}}. \qquad (22)\end{aligned}$$

By integrating (20), (22) is derived as follows:

$$\dot{V}_{\Delta i} \le -\frac{2}{\sigma T_{\mathrm{c}}}\left(2V_{\Delta i} + V_{\Delta i}^{\frac{2-\sigma}{2}} + V_{\Delta i}^{\frac{2+\sigma}{2}}\right).$$

According to Lemma 3, the proposed droop-free unified controller is said to be PdT stable. ■

Remark 4: The PdT stability of the droop-free unified controller implies that the ϑ_i and V_{bus} will converge to $\vartheta_{\mathrm{a}i}$ and V_{nom}, respectively, within the PdT T_{c}.

D. Control Scheme Implementation

Building on the preceding analysis, the detailed implementation of the proposed scheme is illustrated in Fig. 4, taking the ith ESU as an example. As shown, ESU$_i$ obtains status information—namely the virtual variables (ϑ) and the SoCs (S)—from neighboring units via the communication network. A distributed PdT consensus observer is then employed to locally

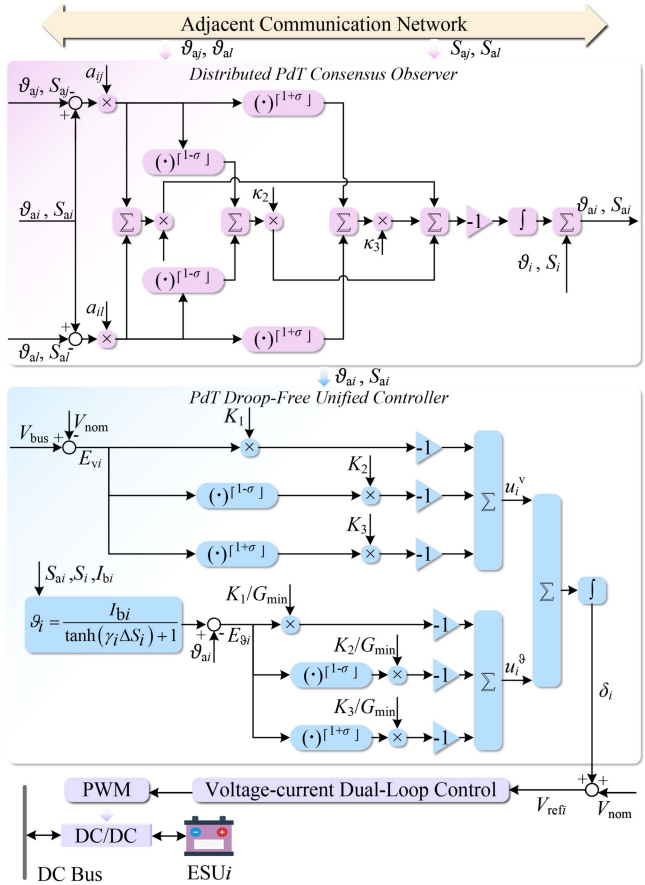

Fig. 4. Detailed schematic diagram of the proposed distributed droop-free unified control scheme.

estimate the average states $\vartheta_{\mathrm{a}i}$ and $S_{\mathrm{a}i}$ within a user-defined convergence time. These estimated averages, along with real-time sampled parameters, such as the bus voltage and output current, are subsequently used to construct the PdT-based droop-free unified controller.

The proposed PdT-based droop-free unified controller simultaneously accomplishes SoC balancing, current sharing, and bus voltage regulation without relying on virtual droop impedance or auxiliary secondary controllers. It produces a regulation signal δ_i to adjust the reference voltage $V_{\mathrm{ref}i}$ of the dual-loop voltage–current control in the dc/dc converter, thereby enabling dynamic duty cycle modulation.

IV. Case Studies

This section evaluates the proposed method's effectiveness and superiority using MATLAB/Simulink. The validation includes bounded settling time comparisons with the FT and adaptive FxT controllers, simulations of communication delays in a ring communication network with CAN bus protocol, assessments under input noise with unequal ESU capacities, system scalability and network expansion analyses, and quantitative performance comparisons with five state-of-the-art methods. These evaluations comprehensively demonstrate the proposed algorithm's performance. The system parameters are detailed in Table II.

TABLE II
SIMULATION AND EXPERIMENTAL SYSTEM PARAMETERS

Item	Parameter	Value
Input voltage of ESUs	$V_{\rm bat1}$,$V_{\rm bat2}$,$V_{\rm bat3}$ (V)	350
Rated bus voltage	$V_{\rm nom}$ (V)	540
Capacitance of converter	C_1,C_2,C_3 (mF)	2
Inductance of converter	L_1,L_2,L_3 (mH)	1
Line conductance of ESU1	G_1 (S)	0.67
Line conductance of ESU2	G_2 (S)	1
Line conductance of ESU3	G_3 (S)	2
Switching frequency	$f_{\rm k}$ (kHz)	20
Predefined settling time	$T_{\rm c}$ (s)	0.1
Communication sampling time	$T_{\rm comn}(\mu{\rm s})$	100
Voltage-loop control parameters	$K_{\rm vp}$, $K_{\rm vi}$	0.5, 8
Current-loop control parameters	$K_{\rm cp}$, $K_{\rm ci}$	0.01, 1
Acceleration factor	ν	0.01
Operational constant	σ	0.5

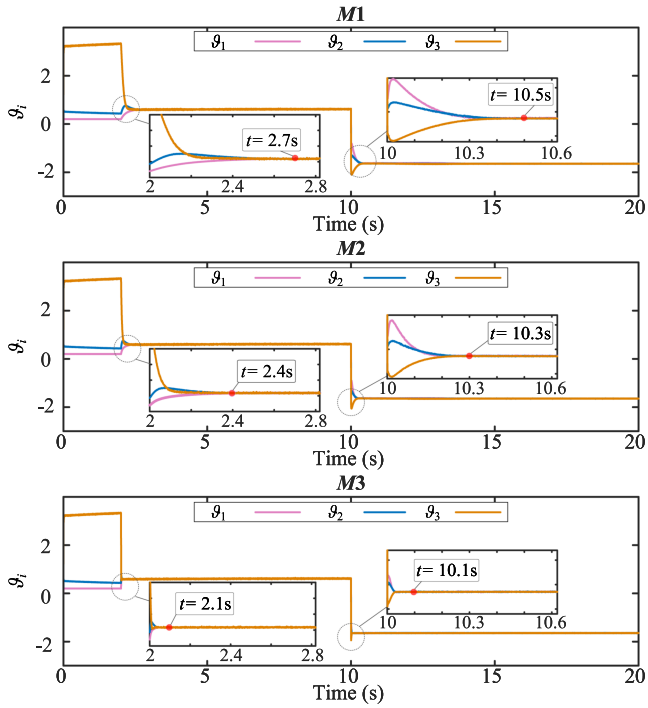

Fig. 5. Comparison results of the convergence performance of ϑ_i between the proposed controller and the FT and adaptive FxT controllers.

A. Case A: Comparison of Bounded Settling Time Under Step Load Disturbance

This case assesses the bounded settling time performance of the proposed scheme in comparison with both FT and adaptive FxT controllers under step load disturbance. The ESUs are initialized with SoC levels of 60%, 55%, and 50%, each having a capacity of 3 Ah. At $t = 10$ s, the power output of the SG rises from 12 to 20 kW, concurrently with a reduction in the power consumption of the CPL from 15 to 12 kW. Figs. 5 and 6 show the simulation results of ϑ_i and $V_{\rm bus}$. In these figures, ***M*1**, ***M*2**, and ***M*3** correspond to the FT controller [20], the adaptive FxT controller [36], and the proposed scheme, respectively. A comparative analysis of the settling times for these controllers is provided in Table III.

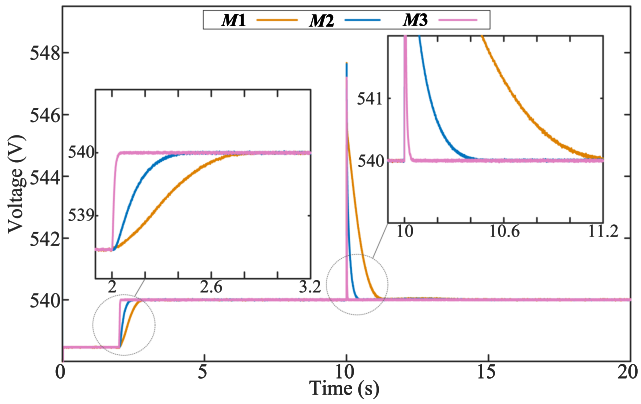

Fig. 6. Comparison results of the $V_{\rm bus}$ regulation performance between the proposed controller and the FT and adaptive FxT controllers.

TABLE III
COMPARISON OF BOUNDED SETTLING TIME OF THE PROPOSED METHOD WITH FT AND ADAPTIVE FXT CONTROLLERS

Method	Settling time	
	$V_{\rm bus}$	ϑ_i
	When control activated	Under load disturbance
FT	0.7 s	0.5 s
Adaptive FxT	0.4 s	0.3 s
Proposed	0.1 s	0.1 s

As observed in Fig. 5, Fig. 6, and Table III, ***M*1** requires 0.7 s to synchronize the virtual state variables upon control activation at 2 s, whereas ***M*2** achieves synchronization within 0.5 s. In addition, ***M*1** takes 0.8 s to restore the bus voltage to its nominal level, while ***M*2** accomplishes this within 0.5 s.

Under step load disturbance at $t = 10$ s, ***M*1** requires 0.5 s to resynchronize the virtual state variables and 1.2 s to restore bus voltage regulation. In contrast, ***M*2** achieves these within 0.3 and 0.5 s, respectively.

In conclusion, the proposed scheme effectively synchronizes the virtual state variables and restores the bus voltage within a user-defined time limit, both at the initial control activation and in response to step load disturbances.

B. Case B: Test of Communication Delay

This case evaluates the reliability of the proposed strategy under communication delays commonly encountered in CAN bus communication networks. Fig. 7(a) and (b) illustrates the simulation results of $I_{{\rm dc}i}$ and $V_{\rm bus}$ for the proposed method under communication delays ($\tau_{\rm d}$) of 5, 30, and 50 ms.

The ESUs are initialized with an SoC of 55%, 40%, and 25%, with a rated capacity of 4Ah. The simulation is divided into three stages as follows.

1) 0–25 s: The power of SG and the CPL are set at 20 and 12 kW, respectively.
2) 25–50 s: The power of the SG and CPL are adjusted to 12 and 15 kW, respectively.
3) 50–60 s: The power settings for the SG and CPL revert to 20 and 12 kW, respectively.

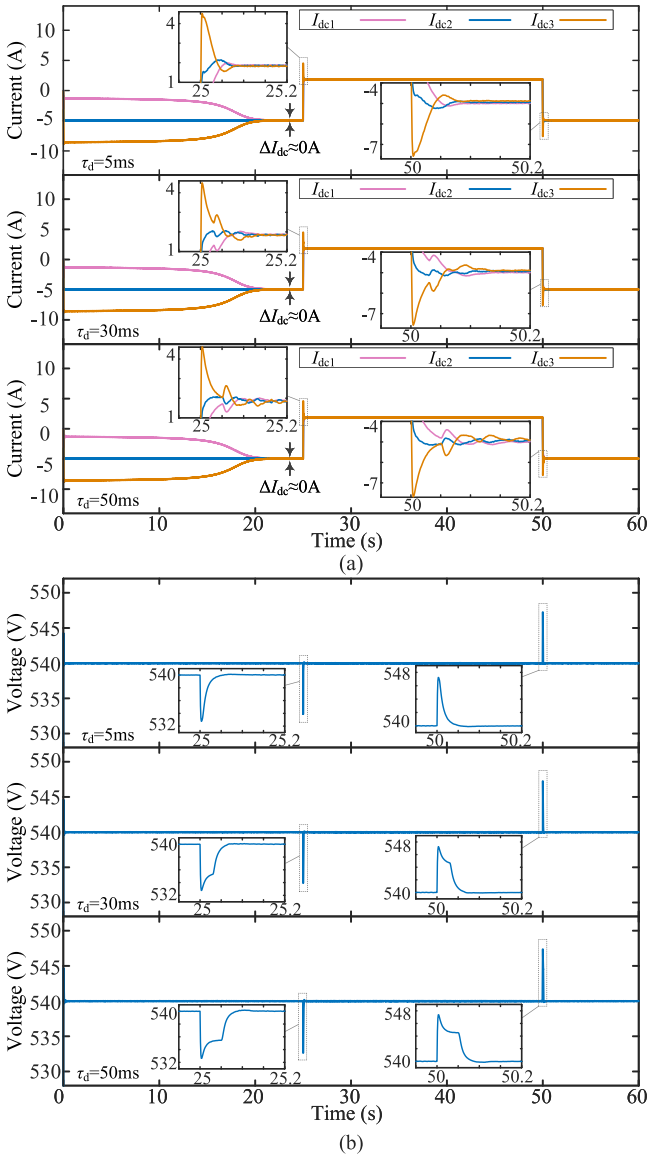

Fig. 7. Simulation results of the proposed scheme under communication delays. (a) Simulation results of $I_{\mathrm{dc}i}$. (b) Simulation results of V_{bus}.

As shown in Fig. 7(a) and (b), 5 ms communication delay has a negligible impact on the control performance of the proposed strategy. The bus voltage recovers to the reference value within 0.1 s. When the delay increases to 30 ms, the ESU output current exhibits minor oscillations under step load disturbances but rapidly returns to a steady state. Meanwhile, the bus voltage recovery slows slightly but remains within 0.1 s.

With a further increase to 50 ms, the ESU output current experiences more pronounced oscillations under step load disturbances and struggles to fully stabilize. In addition, the bus voltage recovery time reaches the user-defined upper limit of 0.1 s. Despite these effects, the predefined control objectives are still met.

Overall, the system maintains adaptive current distribution at $t = 24$ s under communication delays of 5, 30, and 50 ms, ensuring that the bus voltage remains at its nominal value throughout operation. These results confirm that the proposed strategy effectively tolerates communication delays up to 50 ms. In addition, the maximum bus voltage fluctuation amplitude is 7.8 V, ensuring system stability and safety.

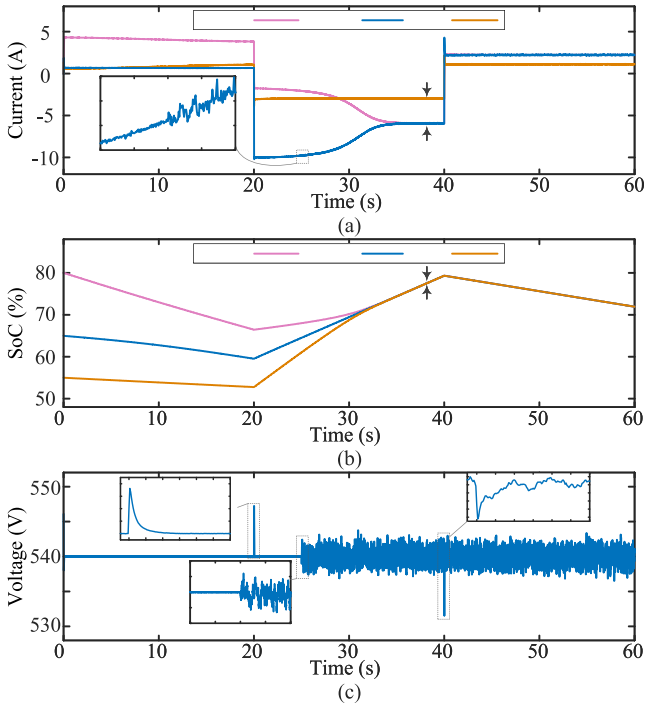

Fig. 8. Simulation results under input noise and unequal capacities. (a) Simulation results of $I_{\mathrm{dc}i}$. (b) Simulation results of S_i. (c) Simulation results of V_{bus}.

C. Case C: Test of Noise Uncertainties and Unequal Capacities

This case study evaluates the effectiveness and robustness of the proposed method under noise conditions. Fig. 8 presents the simulation results, illustrating the output currents, SoC levels of the ESUs, and the bus voltage.

The ESUs are initialized with an SoC of 80%, 65%, and 55%, with a rated capacity of 6, 6, and 3 Ah, respectively. At 25 s, a band-limited white noise signal with a level of 10 dB and a sampling time of 100 μs is introduced into the input of the designed PdT droop-free unified controller ($E_{\vartheta i}$, $E_{\mathrm{V}i}$). The simulation is divided into three stages as follows.

1) 0–20 s: The power of SG and the CPL are set at 12 and 15 kW, respectively.
2) 20–40 s: The power of the SG and CPL are adjusted to 20 and 12 kW, respectively.
3) 40–60 s: The power settings for the SG and CPL revert to 12 and 15 kW, respectively.

As shown in Fig. 8(a) and (b), the output current of the ESUs exhibits high-frequency fluctuations with an amplitude of approximately 0.12 A due to the presence of noise. Despite this, the proposed control strategy successfully achieves precise current allocation based on SoC within 38 s. The SoC balancing error remains close to 0%, and the output current ratio is maintained at 2:2:1.

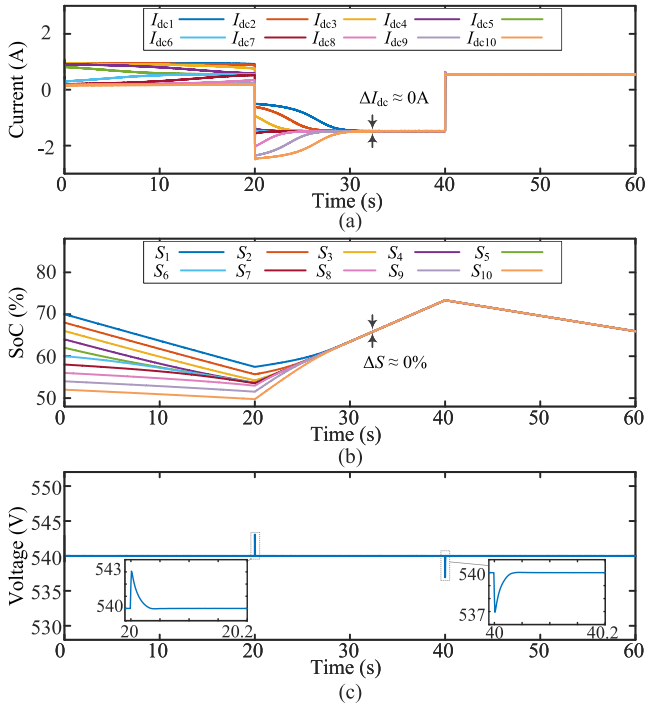

Fig. 9. Simulation results under system and communication network scaling. (a) Simulation results of $I_{\mathrm{dc}i}$. (b) Simulation results of S_i. (c) Simulation results of V_{bus}.

Fig. 8(c) further demonstrates that the noise signal induces high-frequency fluctuations in the bus voltage, with an amplitude of approximately 4 V. Nevertheless, the proposed strategy effectively restores the bus voltage to its nominal value within the user-specified 0.1 s, even in the presence of step load disturbances.

Overall, the presence of noise does not significantly impact the achievement of the control objectives. Although high-frequency fluctuations appear in the output current and bus voltage, their amplitudes remain substantially lower than that of the noise. In addition, the maximum fluctuation amplitude of the bus voltage is limited to 8.2 V, ensuring system stability and operational safety.

D. Case D: Test of Scalability

To validate the scalability of the proposed strategy and network, this case study increases the number of ESUs to 10, while maintaining interconnection via a ring communication network. Fig. 9 presents the simulation results, illustrating the output currents, SoC levels of the ESUs, and the bus voltage.

The ESUs are initialized with SoC levels of 70%, 68%, 66%, 64%, 62%, 60%, 58%, 56%, 54%, and 52%, respectively, each with a rated capacity of 1.5 Ah. The simulation stages remain consistent with those in Case C.

As shown in Fig. 9, despite increasing the number of ESUs and scaling up the network, the proposed strategy successfully achieves SoC balancing and precise current allocation within 32 s, with errors approaching 0% and 0 A, respectively. Under step load disturbances, bus voltage fluctuations remain within 3 V and are restored to the nominal value within the user-defined 0.1 s, ensuring system voltage stability and operational safety.

These results demonstrate that the proposed strategy significantly enhances the scalability of the AEA dc microgrid, maintaining robust performance as the system scales. Moreover, the demonstrated effectiveness suggests that the proposed method holds potential for broader application to other types of dc microgrids with multiple ESUs, such as electric vehicles, ground-based microgrids, and renewable-integrated energy systems.

E. Case E: Compare With State-of-The-Art Mehtods

To further emphasize the performance advantages of the proposed method, this case study conducts a comparative analysis against five state-of-the-art approaches. Table IV presents the quantitative performance comparison between the proposed method and the benchmark methods, where ***M*1** to ***M*5** correspond to the methods proposed in [12], [17], [19], [22], and [26], respectively. The reference time point for this evaluation, denoted as T_{ref} is set at 39 s.

The ESUs are initialized with SoC levels of 65%, 50%, and 40%, respectively, each with a rated capacity of 6 Ah. The simulation stages remain consistent with those in Case C.

The results in Table IV validate the effectiveness of the proposed method in achieving SoC-based current allocation within T_{ref}. The bus voltage fluctuation remains below 7.2 V and is regulated to the reference value within 0.1 s.

Compared to the droop-free control strategy (***M*5**), the proposed method achieves a comparable voltage fluctuation amplitude while ensuring SoC-based current allocation. In contrast, ***M*5** fails in this regard, resulting in an SoC difference of 25.4% at T_{ref}, indicating divergence in battery SoC during operation. This underscores that, beyond meeting the predefined convergence speed, the proposed method effectively enables SoC-based power allocation, a capability unattainable with existing droop-free strategies.

Against improved droop control-based methods, the proposed method exhibits superior performance. At T_{ref}, ***M*1**, ***M*2**, and ***M*3** show significant SoC and current deviations, whereas the proposed method achieves faster SoC balancing and higher current allocation accuracy. Moreover, it reduces voltage fluctuation by 80.8%, 25.8%, and 60.4% compared to ***M*1**, ***M*2**, and ***M*3**, respectively, while achieving faster voltage regulation. Compared to ***M*4**, the proposed method achieves a similar SoC balancing speed but reduces voltage fluctuation by 68%, enhancing system voltage stability and operational safety.

Overall, the proposed method delivers the best performance, combining SoC-based power allocation with superior voltage regulation, thereby improving system efficiency and reliability.

V. Experimental Results

To validate the effectiveness of the proposed distributed PdT droop-free unified control scheme, a StarSim-based AEA dc microgrid experimental platform was established, as illustrated in Fig. 10. The power circuit, comprising three groups of ESUs, SGs, and propulsion loads, is simulated in real time using

TABLE IV
PERFORMANCE COMPARISON BETWEEN THE PROPOSED METHOD AND THE STATE-OF-THE-ART METHODS

Performance \ Method	***M1*** (2017)	***M2*** (2018)	***M3*** (2022)	***M4*** (2024)	***M5*** (2022)	Proposed
Dependency on droop control	Droop-based	Droop-based	Droop-based	Droop-based	Droop-free	Droop-free
SoC balancing error at T_{ref}	5.1%	10.4%	1.5%	0%	25.4%	0%
Current distribution error at T_{ref}	2.7 A	2.9 A	1.5 A	0 A	0 A	0 A
Maximum voltage fluctuations amplitude	37.5 V	9.7 V	18.2 V	22.5 V	7.9 V	7.2 V
Voltage regulation time under load disturbances	0.3 s	0.4 s	0.3 s	0.3 s	0.2 s	0.1 s

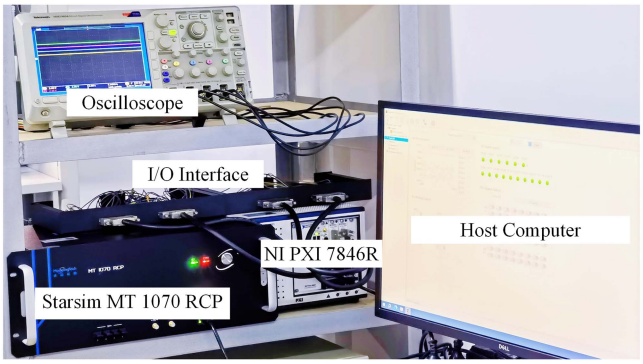

Fig. 10. Starsim experimental validation platform based on NI PXIe-7846R and MT 1070.

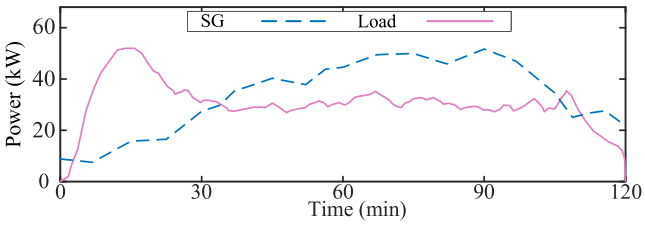

Fig. 11. Load and SG power profiles for a two-hour flight mission.

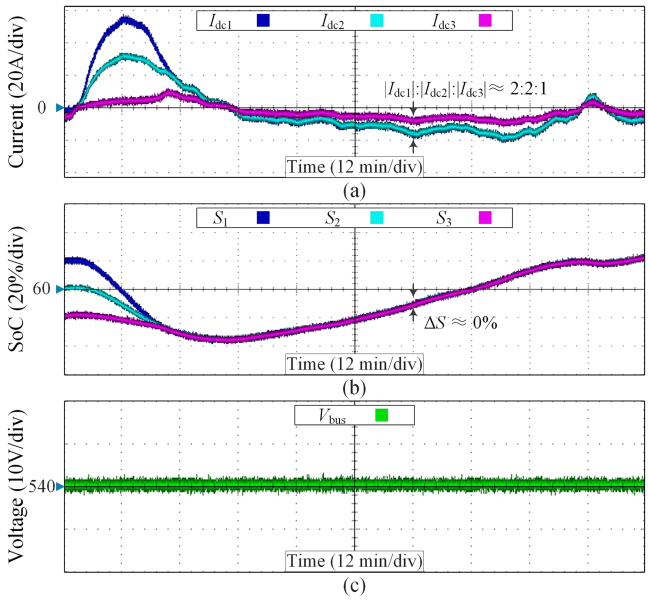

Fig. 12. Experimental results under inconsistent ESU capacities. (a) Experimental results of $I_{\text{dc}i}$. (b) Experimental results of S_i. (c) Experimental results of V_{bus}.

an NI PXIe-7846R platform equipped with a Kintex-7 160 T programmable FPGA, operating with a simulation time step of 1 μs. The control algorithm is deployed on an MT-1070 rapid control prototyping device, which features a dual-core ARM Cortex-A9 processor (800MHz) and operates with a sampling and control period of 100 μs. Data exchange between the NI PXIe-7846R and MT-1070 is facilitated via I/O interfaces, while a host computer is used to monitor and manage the operation of the AEA dc microgrid in real time. The system parameters are listed in Table II.

As illustrated in Fig. 11, the platform emulates a 50-kW-class, twp-hour flight mission, encompassing aircraft takeoff, cruising, landing phases, and SGs with fluctuating generation. This mission is designed to validate the proposed strategy's effectiveness in real-world power demand scenarios.

A. Case I: Unequal Proportional Current Distribution

This case evaluates the proposed strategy's performance under fluctuating load and SG generation conditions, considering unequal ESU capacities.The ESUs are initialized at SoC levels of 80%, 60%, and 40%, with capacities of 24, 24, and 12 Ah, respectively—reflecting typical variations in real-world systems due to manufacturing or aging.

Fig. 12(a)–(c) displays the experimental results for $I_{\text{dc}i}$, S_i, and V_{bus}, respectively. The proposed method achieves rapid SoC balancing even with substantial initial SoC variations among ESUs. By $t = 30$ min, dynamic SoC balancing ($\Delta S \approx 0\%$) is achieved, and ESU currents are allocated in a 2:2:1 ratio according to their capacities. Furthermore, as shown in Fig. 12(c), the proposed method maintains bus voltage at approximately 540 V despite load and generation fluctuations. These results demonstrate the method's capability to handle practical mismatches in capacity and operating conditions, enhancing system operational safety.

B. Case II: Premature Exit of ESU

This case evaluates the effectiveness of the proposed control strategy in maintaining energy storage system reliability amid an ESU failure. The ESUs are initialized with SoC levels of 60%, 50%, and 40%, each with a capacity of 24 Ah. ESU3 malfunctions and exits the system at $t = 90$ min.

Fig. 13(a)–(c) presents the experimental results for $I_{\text{dc}i}$, S_i, and V_{bus}, respectively. By $t = 15$ min, dynamic SoC balancing is achieved with near-zero error, ensuring precise current allocation. Upon ESU3's exit at an SoC of approximately 51%,

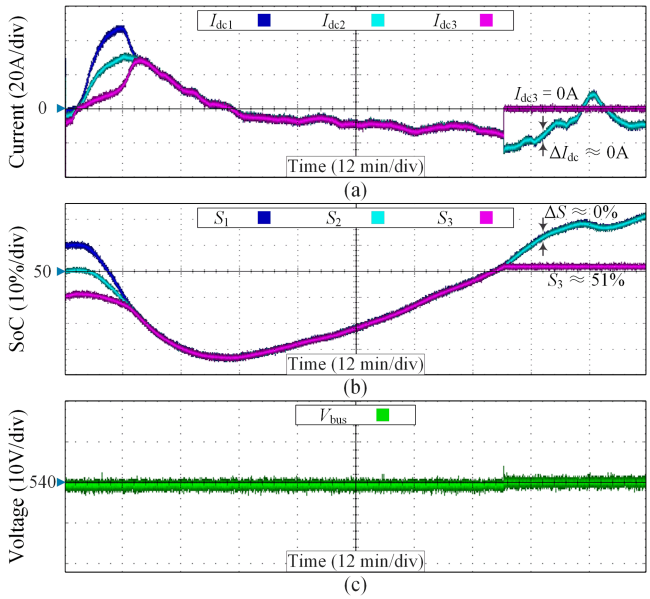

Fig. 13. Experimental results under the condition of ESU premature exit from operation. (a) Experimental results of I_{dci}. (b) Experimental results of S_i. (c) Experimental results of V_{bus}.

the SoC balancing and current distribution of the remaining ESUs remain unaffected, demonstrating the proposed method's robustness against equipment failures. As shown in Fig. 13(c), even under failure conditions, the proposed strategy maintains bus voltage fluctuations within 5 V and stabilizes the bus voltage at approximately 540 V, significantly enhancing system stability and reliability. These capabilities are crucial for real-world AEA systems, where unexpected ESU disconnections or faults may occur during flight.

C. Case III: Comparative Analysis

This case study evaluates the performance of the proposed method against an advanced benchmark in a practical application scenario. The assessment focuses on SoC balancing, current distribution, and bus voltage regulation, highlighting the advantages of the proposed approach. Experimental results are presented in Fig. 14, where ***M*1** represents the method in [12] ($p = 8$, $R_D = 0.6\Omega$). The ESUs are initialized with SoC levels of 80%, 60%, and 40%, each with a capacity of 24 Ah.

Fig. 14(a) and (b) compares ***M*1** and the proposed method in terms of SoC balancing and current distribution. At $t = 30$ min, the proposed method achieves rapid and precise current allocation based on SoC levels. In contrast, although ***M*1** employs an SoC-aware adaptive droop control strategy, its performance is significantly affected by line impedance variations. Consequently, ***M*1** fails to achieve satisfactory SoC balancing and current distribution throughout the simulated flight mission, exhibiting errors of approximately 16 A in current distribution and 20% in SoC balancing at the same instant. In comparison, the proposed method reduces both errors to near-zero levels. These results demonstrate the proposed method's superior speed and accuracy in SoC-based current distribution, as well as its robustness against line impedance mismatches. Such improvements

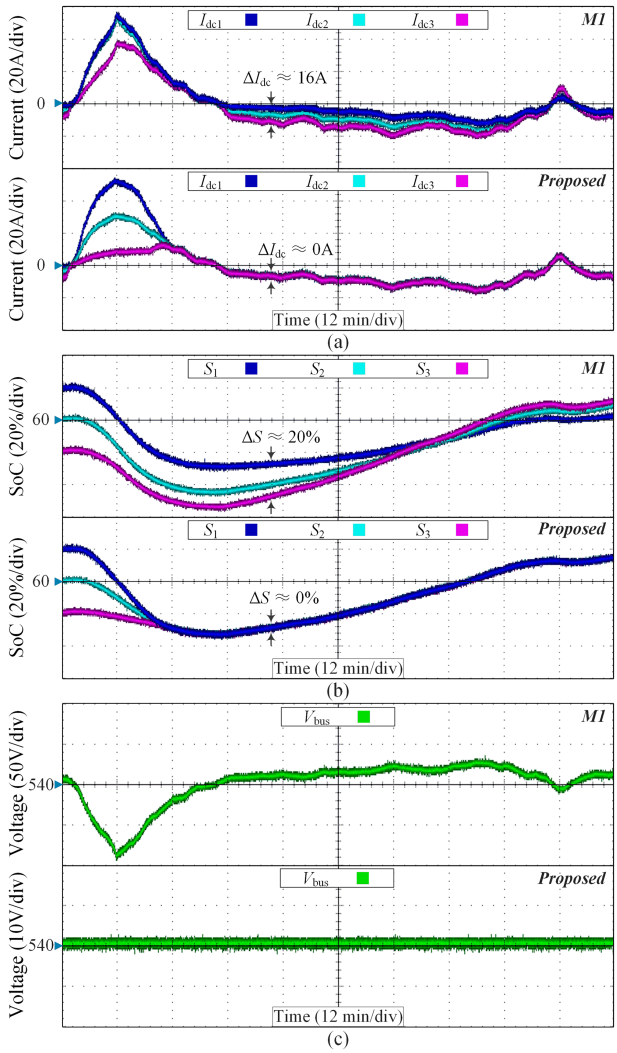

Fig. 14. Comparison experimental results between the proposed method and that in [12]. (a) Experimental results of I_{dci}. (b) Experimental results of S_i. (c) Experimental results of V_{bus}.

help reduce energy imbalance among onboard battery packs, extend their operational lifespan, and minimize the need for frequent maintenance—benefits that are particularly valuable in mission-critical AEA systems.

Fig. 14(c) further compares the bus voltage regulation capabilities of ***M*1** and the proposed method. Despite using a smaller initial droop coefficient, ***M*1** experiences significant bus voltage deviations due to elevated system power demand, with deviations reaching up to 90 V under worst-case conditions, posing a potential risk to operational safety. In contrast, the proposed method maintains bus voltage tightly regulated around the nominal 540 V throughout the mission. These results confirm the proposed method's superior capability in ensuring voltage stability compared to the advanced benchmark. In real-world applications, such tight voltage regulation reduces the risk of triggering protection mechanisms, ensures stable operation of avionics and propulsion loads, and contributes to the overall electrical safety of AEA platforms.

VI. Conclusion

This article presents a novel distributed PdT droop-free unified control scheme to address SoC imbalance, inaccurate current distribution, and dc bus voltage deviations in multi-ESU onboard dc microgrids for AEA. The scheme combines a distributed PdT consensus observer, enabling local estimation of global averages within a user-defined time, with a unified controller that integrates multiple control objectives into a cohesive framework. Robustness and scalability are verified through simulations under communication delays, input noise, and varying system scales, confirming stable performance under practical uncertainties. Owing to its concise structure, the approach is also applicable to other dc microgrids, such as those in electric vehicles, ground-based systems, and renewable-integrated networks. Comparative simulations in MATLAB/Simulink show that the proposed scheme achieves fast synchronization of virtual variables and bus voltage recovery within PdT limits. Compared to existing droop-free methods, it enhances fast SoC-based current sharing; relative to improved droop-based strategies, it reduces bus voltage fluctuation by up to 80.8% while improving SoC balancing and current allocation accuracy. Real-time experiments on the Starsim platform under varied scenarios further validate the method's practical feasibility, robustness, and suitability for real-world AEA applications.

Future research will focus on enhancing the proposed droop-free unified control scheme by addressing its current limitations. Key directions include improving resilience against cyberthreats and extreme communication failures, as well as integrating battery state-of-health considerations to extend system longevity and reliability. In addition, efforts will be directed toward the real-time implementation of the proposed strategy on practical platforms.

References

[1] A. Barzkar and M. Ghassemi, "Components of electrical power systems in more and all-electric aircraft: A review," *IEEE Trans. Transp. Electrif.*, vol. 8, no. 4, pp. 4037–4053, Dec. 2022.

[2] Z. Zuo et al., "Finite-time tracking control with fast reaching condition for disturbed more electric aircraft direct current microgrid with constant power loads," *IEEE Trans. Aerosp. Electron. Syst.*, vol. 59, no. 5, pp. 6695–6704, Oct. 2023.

[3] D. Lawhorn, V. Rallabandi, and D. M. Ionel, "Multi-objective optimization for aircraft power systems using a network graph representation," *IEEE Trans. Transp. Electrif.*, vol. 7, no. 4, pp. 3021–3031, Dec. 2021.

[4] B. Sarlioglu and C. T. Morris, "More electric aircraft: Review, challenges, and opportunities for commercial transport aircraft," *IEEE Trans. Transp. Electrif.*, vol. 1, no. 1, pp. 54–64, Jun. 2015.

[5] Y. Zeng et al., "Distributed unified controller design for parallel battery storage system in DC shipboard microgrid," *IEEE Trans. Power Syst.*, vol. 39, no. 1, pp. 546–563, Jan. 2024.

[6] Z. Chen et al., "Hierarchical state-of-charge balancing and second-harmonic current suppressing control with a scalable DC reconfigurable battery pack," *IEEE Trans. Power Electron.*, vol. 39, no. 6, pp. 6758–6768, Jun. 2024.

[7] S. Peyghami et al., "Synchronverter-enabled DC power sharing approach for LVDC microgrids," *IEEE Trans. Power Electron.*, vol. 32, no. 10, pp. 8089–8099, Oct. 2017.

[8] X. Lu et al., "Double-quadrant state-of-charge-based droop control method for distributed energy storage systems in autonomous DC microgrids," *IEEE Trans. Smart Grid*, vol. 6, no. 1, pp. 147–157, Jan. 2015.

[9] X. Lu et al., "State-of-charge balance using adaptive droop control for distributed energy storage systems in DC microgrid applications," *IEEE Trans. Ind. Electron.*, vol. 61, no. 6, pp. 2804–2815, Jun. 2014.

[10] C. Li et al., "Voltage scheduling droop control for state-of-charge balance of distributed energy storage in DC microgrids," in *Proc. IEEE Int. Energy Conf. (ENERGYCON)*, May 2014, pp. 1310–1314.

[11] N. Zhi et al., "An SOC-based virtual DC machine control for distributed storage systems in DC microgrid," *IEEE Trans. Energy Convers.*, vol. 35, no. 3, pp. 1411–1420, Sep. 2020.

[12] T. R. Oliveira, W. W. A. Goncalves Silva, and P. F. Donoso-Garcia, "Distributed secondary level control for energy storage management in DC microgrids," *IEEE Trans. Smart Grid*, vol. 8, no. 6, pp. 2597–2607, Nov. 2017.

[13] P. Wang et al., "An improved distributed secondary control method for DC microgrids with enhanced dynamic current sharing performance," *IEEE Trans. Power Electron.*, vol. 31, no. 9, pp. 6658–6673, Sep. 2016.

[14] K. D. Hoang and H.-H. Lee, "Accurate power sharing with balanced battery state of charge in distributed DC microgrid," *IEEE Trans. Ind. Electron.*, vol. 66, no. 3, pp. 1883–1893, Mar. 2019.

[15] Y. Zeng et al., "Hierarchical cooperative control strategy for battery storage system in islanded DC microgrid," *IEEE Trans. Power Syst.*, vol. 37, no. 5, pp. 4028–4039, Sep. 2022.

[16] Y. Mi et al., "Accurate power allocation of multienergy storage island DC microgrid based on virtual power rating," *IEEE Trans. Power Electron.*, vol. 38, no. 1, pp. 261–270, Jan. 2023.

[17] X. Chen et al., "Distributed cooperative control and stability analysis of multiple DC electric springs in a DC microgrid," *IEEE Trans. Ind. Electron.*, vol. 65, no. 7, pp. 5611–5622, Jul. 2018.

[18] Y. Zeng et al., "An improved distributed secondary control strategy for battery storage system in DC shipboard microgrid," *IEEE Trans. Ind. Appl.*, vol. 58, no. 3, pp. 4062–4075, May–Jun. 2022.

[19] B. Huang et al., "Distributed optimal control of DC microgrid considering balance of charge state," *IEEE Trans. Energy Convers.*, vol. 37, no. 3, pp. 2162–2174, Sep. 2022.

[20] R. Zhang and B. Hredzak, "Distributed finite-time multiagent control for DC microgrids with time delays," *IEEE Trans. Smart Grid*, vol. 10, no. 3, pp. 2692–2701, May 2019.

[21] S. Sahoo et al., "A distributed fixed-time secondary controller for DC microgrid clusters," *IEEE Trans. Energy Convers.*, vol. 34, no. 4, pp. 1997–2007, Dec. 2019.

[22] Y. Zeng et al., "Fixed-time secondary controller for rapid state-of-charge balancing and flexible bus voltage regulation in DC microgrids," *IEEE Trans. Power Syst.*, vol. 39, no. 3, pp. 5393–5407, May 2024.

[23] W. Yang et al., "Predefined-time observer-based fast power allocation for battery energy storage systems," *IEEE Trans. Circuits Syst. II- Exp. Briefs*, vol. 71, no. 10, pp. 4506–4510, Oct. 2024.

[24] H. Wu et al., "Prescribed-time control for DC microgrids with battery energy storage systems," *IEEE Trans. Ind. Inform.*, vol. 20, no. 10, pp. 11896–11907, Oct. 2024.

[25] S. Moayedi et al., "Team-oriented load sharing in parallel DC–DC converters," *IEEE Trans. Ind. Appl.*, vol. 51, no. 1, pp. 479–490, Jan./Feb. 2015.

[26] Q. Zhang et al., "Droop-free distributed cooperative control framework for multisource parallel in seaport DC microgrid," *IEEE Trans. Smart Grid*, vol. 13, no. 6, pp. 4231–4244, Nov. 2022.

[27] F. Guo et al., "Distributed secondary control for power allocation and voltage restoration in islanded DC microgrids," *IEEE Trans. Sustain. Energy*, vol. 9, no. 4, pp. 1857–1869, Oct. 2018.

[28] Y. Dou et al., "Distributed secondary control for voltage regulation and optimal power sharing in DC microgrids," *IEEE Trans. Control Syst. Technol.*, vol. 30, no. 6, pp. 2561–2572, Nov. 2022.

[29] F. Aalipour and T. Das, "Proportional power-sharing control of distributed generators in microgrids," *IEEE Trans. Control Syst. Technol.*, vol. 30, no. 2, pp. 481–494, Mar. 2022.

[30] Z. Zuo and L. Tie, "Distributed robust finite-time nonlinear consensus protocols for multi-agent systems," *Int. J. Syst. Sci.*, vol. 47, no. 6, pp. 1366–1375, Jun. 2014.

[31] L. Wang and F. Xiao, "Finite-time consensus problems for networks of dynamic agents," *IEEE Trans. Autom. Control*, vol. 55, no. 4, pp. 950–955, Apr. 2010.

[32] M. Zhang, H. Zang, and L. Bai, "A new predefined-time sliding mode control scheme for synchronizing chaotic systems," *Chaos Solitons Fractals*, vol. 164, pp. 112745–112745, Nov. 2022.

[33] B. Ning et al., "Fixed-time and prescribed-time consensus control of multiagent systems and its applications: A survey of recent trends and methodologies," *IEEE Trans. Ind. Inform.*, vol. 19, no. 2, pp. 1121–1135, Feb. 2023.

[34] Z. Fan, B. Fan, and W. Liu, "Distributed control of DC microgrids for optimal coordination of conventional and renewable generators," *IEEE Trans. Smart Grid*, vol. 12, no. 6, pp. 4607–4615, Nov. 2021.
[35] J. Peng, B. Fan, and W. Liu, "Voltage-based distributed optimal control for generation cost minimization and bounded bus voltage regulation in DC microgrids," *IEEE Trans. Smart Grid*, vol. 12, no. 1, pp. 106–116, Jan. 2021.
[36] P. Wang et al., "An adaptive fixed-time cascaded distributed control for bipolar-type DC microgrids considering time delays," *IEEE Trans. Ind. Electron.*, vol. 71, no. 11, pp. 14764–14775, Nov. 2024.

Heyang Yu was born in Liaoning, China, in 1999. He received the M.S. degree in marine engineering from Dalian Maritime University, Dalian, China, in 2024. He is currently working toward the Ph.D. degree in control science and engineering with the Dalian University of Technology, Dalian, China.

His research interests include electric–hydrogen hybrid microgrids for aircraft, energy storage systems, distributed cooperative control, and energy management.

Ping Lin was born in Chongqing, China. He received the Ph.D. degree in navigation guidance and control from the School of Control Science and Engineering, Dalian University of Technology, Dalian, China, in 2021.

Since 2024, he has been an Associate Professor with the School of Control Science and Engineering, Dalian University of Technology. His research interests include nonlinear systems, active disturbance rejection control, and generator control systems.

Yuji Zeng (Graduate Student Member, IEEE) was born in Guangdong, China, in 1996. He received the B.S. degree in marine engineering from Guangdong Ocean University, Zhanjiang, China, in 2018. He is currently working toward the Ph.D. degree in marine engineering with Dalian Maritime University, Dalian, China.

He is a Visiting Ph.D. Student with the Department of Electrical, Electronic and Computer Engineering, School of Engineering, The University of Western Australia, Perth, WA, Australia. His research interests include shipboard hybrid power systems, dc microgrids, fuel cell systems, energy storage systems, distributed cooperative control, and energy management.

Qinjin Zhang (Member, IEEE) was born in Jiangsu, China, in 1986. He received the B.S. degree in electrical engineering and automation from Dalian Maritime University, Dalian, China, in 2009, the M.S. and Ph.D. degrees in marine engineering from Dalian Maritime University, Dalian, China, in 2011 and 2015, respectively.

Since 2020, he has been an Associate Professor with the School of Marine Engineering, Dalian Maritime University, Dalian, China. His research interests include distributed energy generation technology, power electronics converters, microgrids, and ship dc integrated power system.

Yuhu Wu (Member, IEEE) received the Ph.D. degree in mathematics from the Harbin Institute of Technology, Harbin, China, in 2012.

In October 2015, he joined the School of Control Science and Engineering, Dalian University of Technology, Dalian, China, where he is currently a Professor. His research interests include nonlinear control theory, game-theoretic control, and the application of control techniques to automotive powertrain systems and unmanned aerial vehicles.